Applied Catalysis B: Environmental 165 (2015) 537–546

Contents lists available at ScienceDirect

Applied Catalysis B: Environmental

journal homepage: www.elsevier.com/locate/apcatb

Understanding of the effect of synthesis temperature on the crystallization and activity of nano-MoS_2 catalyst

Haiping Zhang[a], Hongfei Lin[a], Ying Zheng[a,*], Yongfeng Hu[b], Aimee MacLennan[b]

[a] Department of Chemical Engineering, University of New Brunswick, 15 Dineen Drive, Fredericton, NB, E3B 5A3, Canada
[b] Canadian Light Source Inc., 44 Innovation Boulevard, Saskatoon, SK, S7N 2V3, Canada

ARTICLE INFO

Article history:
Received 16 July 2014
Received in revised form 16 October 2014
Accepted 19 October 2014
Available online 27 October 2014

Keywords:
Unsupported MoS_2
Hydrothermal
Synthesis temperature
Initial temperature
Hydrodesulfurization (HDS)
Light cycle oil

ABSTRACT

Temperature is a key factor in the hydrothermal synthesis of MoS_2 with high catalytic activity. In this paper, the effect of synthesis temperature (sTemp) and initial temperature (iTemp) was carefully investigated against catalyst crystal structure and hydrotreating activities. The synthesized nano-MoS_2 was extensively characterized and evaluated using light cycle oil. There is a minimum sTemp for the formation of crystalline MoS_2. Temperatures lower than the minimal sTemp result in amorphous structures. Surpassing this temperature leads to crystallization which goes through different growth routes. Higher iTemp promotes fast nucleation and thus nuclei combination growth. This leads to shorter slabs with a larger degree of defects, and a higher hydrotreating activity. At lower iTemp, crystal tends to grow in a continous way, resulting in fewer defects. In this way, with the increased sTemp, crystallinity is enhanced and slabs are curved and shortened. Both effects lead to improved hydrotreating performances.

1. Introduction

Recent environmental regulations that are becoming more heavily stringent on the sulfur content in the transportation fuels are signaling for new hydrodesulfurization (HDS) catalysts with higher deep desulfurization activity [1,2]. Unsupported MoS_2-based catalysts with a high density of active sites have a great potential for the improvement of HDS performance [3,4]. It is reported that the unsupported catalysts, e.g., commercialized NEBULA catalysts, are more active in deep HDS than the conventional supported catalysts [4–7]. Thus, study on the preparation of dispersed MoS_2 is a promising research direction.

Nanocrystalline MoS_2 can be synthesized by a variety of techniques, and hydrothermal method is one of the desirable approaches [8–10]. In this technique, temperature is a key factor in controlling nucleation and crystal growth. External energy (heating) is needed to overcome the activation energy barriers for the nucleation and consequent growth. Meanwhile, activation energy of different crystal facets is also affected by temperature through the effect on interfacial energy [11]. In addition, variation of crystallization temperature changes the equilibrium solubility of the subjected material, i.e., the supersaturation state. An elevated supersaturation would significantly enhance the growth on a preferred surface [12]. Through the control of crystallization, temperature can further influence the crystallinity, crystalline size, and morphology [13–16]. It is reported that crystalline MoS_2 cannot be generated at too low or high temperatures [9,10]. In a low temperature range of 120–150 °C, only amorphous MoS_2 nanospheres were observed without any layered crystalline structure present [17]. When MoS_2 was successfully produced, the morphology and crystalline size can also be largely affected by temperature. The trend that increasing temperature led to larger particle sizes was found between 230 and 260 °C by Li et al. with different morphologies observed [10]. At high temperature range 300–375 °C, on the other hand, the sizes of promoted MoS_2 crystalline decrease with increasing temperature. The morphology also changed with temperature as given by an increased curvature of MoS_2 slabs [18].

However, although several investigations have been performed on the hydrothermal conditions of MoS_2 synthesis, there is lack of systematic study on temperature effect. From a catalysis view, a comprehensive study of the effect of temperature is yet not conducted. In our previous work, a novel one-step hydrothermal technique was established for preparation of dispersed MoS_2 using commercially available MoO_3 and Na_2S as precursors [19]. The present work focuses on the effect of temperature on MoS_2 properties and activities. Both synthesis temperature and initial temperature were investigated. The properties of MoS_2 catalysts synthesized at different temperatures were extensively

* Corresponding author. Tel.: +1 506 447 3329.
E-mail address: yzheng@unb.ca (Y. Zheng).

http://dx.doi.org/10.1016/j.apcatb.2014.10.046
0926-3373/

Table 1
Synthesis conditions and textural structure of synthesized catalysts.

Catalysts	Synthesis conditions		Average slab length, L (nm)	Average slab thickness, T (nm)	L/T ratio[c]	BET surface area (m^2/g)
	iTemp[a] (°C)	sTemp[b] (°C)				
CAT-20-200	20	200	10.2/12.6[d]	5.1/4.8[d]	2.0	84.5
CAT-20-270	20	270	13.4/13.6[d]	1.9/1.9[d]	7.1	218.4
CAT-20-320	20	320	17.9/18.2[d]	2.5/2.5[d]	7.2	198.9
CAT-20-350	20	350	11.3	2.0	5.7	155.9
CAT-270-320	270	320	12.3	1.7	7.3	236.3
CAT-270-320*	270	320	7.9	1.1	7.2	261.9

[a] iTemp: Initial temperature at which the heating starts.
[b] sTemp: Synthesis temperature at which synthesis maintains.
[c] L/T ratio: Ratio of average slab length to slab thickness.
[d] The crystalline size of spent catalysts after 8 h hydrotreatment.

characterized by TEM, BET, XRD, XPS, TPR, and XAFS, etc.; the hydrotreatment activities were evaluated using light cycle oil (LCO). A relationship is also attempted to build between the syntheses conditions to catalysts structure and activity.

2. Experimental

2.1. Catalyst synthesis

A series of molybdenum sulfide catalysts were synthesized via a hydrothermal method in a 1000 ml stainless steel autoclave (Parker Autoclave Engineers). 5.436 g of MoO_3 (STEM Scientific) and 33.989 g of $Na_2S{\cdot}9H_2O$ (Fisher Scientific) were first dissolved in 300 ml deionized water after which, 42.5 ml of 4 M HCl solution (Fisher Scientific) was slowly added. The molar ratio of precursors was 1: 3.75: 4.5. The synthesis reaction occurred at different temperatures in the range of 200–350 °C. For the synthesis temperature of 320 °C, two initial temperatures of 20 °C and 270 °C were investigated. A special heating protocol was applied for the higher initial temperature (270 °C). The reactor, containing 300 ml water, was first preheated to 270–280 °C. Sixty milliliter of concentrated precursor solution was then instantaneously injected into the reactor by nitrogen drive to achieve the high-temperature start-up. For a special run, an immediate shutdown was applied once the reactor hits the setting temperature 320 °C. All the other synthesis runs lasted for 2 h under the stirring of 500 rpm unless indicated. After each run, the reactor was immediately cooled down with cooling water.

Black solid residue, which resulted from synthesis, was filtered and carefully washed with distilled water and ethanol. Catalysts prepared at different temperatures were denoted as CAT-initial temperature-synthesis temperature, e.g., CAT-20-200 stands for catalysts prepared at 200 °C with an initial temperature of 20 °C (room temperature). A suffix "*" was used to indicate immediately suspended run at time zero, e.g., CAT-270-320*. The conditions are listed in Table 1.

2.2. Catalyst characterization

Nitrogen adsorption–desorption isotherms were measured at 77 K using an Autosorb-1 (Quantachrome Instruments, Florida, US). The specific surface area of the catalyst powder was calculated using the Brunauer–Emmett–Teller (BET) method with linear region in the P/Po range of 0.10–0.30. Pore size distribution of the catalyst powder was determined from the isotherms via the Barrett–Joyner–Halenda (BJH) method. X-ray diffractograms were recorded on a diffractometer (Bruker AXS D8 XRD) using CuKα radiation. For all the samples, the 2θ range was 5–85° and the scan speed was 1°/min. The morphology of catalysts was measured with TEM (JEOL 2011 STEM, JEOL Ltd., Tokyo, Japan). The length and thickness of crystals were determined using image analysis software and the averages were calculated based on at least 200 MoS_2 crystals measured from different particles according to Eqs. (1) and (2). The morphology of catalyst particles was observed using scanning electron microscopy (JEOL JSM6400 SEM). The atomic ratio of the catalyst was estimated by energy dispersive X-ray emission (EDX) coupled with TEM.

$$\text{Average slab thickness } \bar{T} = \frac{\sum_{i=1,2\ldots n}^{n} T_i}{n} \quad (1)$$

$$\text{Average slab thickness } \bar{L} = \frac{\sum_{i=1,2\ldots n}^{n} L_i N_i}{\sum_{i=1,2\ldots n}^{n} N_i} \quad (2)$$

where L, T, and N stand for slab length, slab thickness, and number of layers in each crystal, respectively.

Temperature-programmed reduction (TPR) was conducted on Autosorb-1 (Quantachrome Instruments, Florida, US). Approximately, 100 mg catalyst was placed in a quartz U-tube and reduced by heating from room temperature to 700 °C at a rate of 10 °C/min under a 50 ml/min flow of 2% H_2/Ar. The consumption of H_2 was recorded using a mass spectrometer (RGA 200 Stanford Research Systems, Inc.).

XPS spectra of Mo3d and S2p were recorded using an AXIS 165 spectrometer (Kratos Analytical) equipped with a 210 W Al Kα monochromatic source ($h\nu$ = 1486.6 eV). The resolution of the instrument is 0.55 eV for Ag 3d and 0.70 eV for Au 4f peaks. Sample preparation was carried out under an Ar atmosphere to avoid oxidization. The survey scans were collected for binding energy extending from 1100 eV to 0 with analyzer pass energy of 160 eV and a step of 0.4 eV and the high-resolution spectra were collected at a pass energy of 20 eV with a step of 0.1 eV.

The X-ray absorption near-edge structure (XANES) of S K-edge and Mo L3-edge was measured at the Soft X-ray Microanalysis Beamline (SXRMB) of the Canadian Light Source (CLS; Saskatoon, SK, Canada). The spectra were recorded in a total electron yield mode at room temperature using a Si (111) double crystal monochromator. Data analysis of the XANES spectra was performed using Athena software. The extended X-ray absorption fine structure (EXAFS) spectra of Mo K-edge were recorded in the transmission mode at room temperature. The structure parameters around Mo were obtained by Fourier transformation using FEFF 6 software. Detailed procedure was described elsewhere [20,21].

2.3. Evaluation of unsupported catalysts

A batch reactor from Parker Autoclave Engineers was employed in this experiment. Light cycle oil with 1.5 wt% S and 159 ppm N was selected as the feedstock. 0.6 g catalyst filtered through 200 meshes was added into autoclave. After heating the reactor to 375 °C, 120 g LCO was introduced into the reactor, making the weight

ratio of catalyst to oil 1:200. The hydrodesulfurization (HDS) and hydrodenitrogenation (HDN) took place at 375 °C under 1400–1500 psi pressure.

The sulfur and nitrogen content in the original LCO and hydrotreated products were determined using a Sulfur/Nitrogen analyzer (9000 series, Antek Instruments Inc). A detailed sulfur compounds composition was analyzed by gas chromatography equipped with a non-polar VF-1ms capillary column (15 m × 0.25 mm × 0.25 μm, max temperature: 325 °C) and a PFPD detector (Varian 450). The following temperature profile was used: 2 min at 120 °C, followed by a linear increase at 6 °C/min to 170 °C and another increase at 20 °C/min to 290 °C, held for 2 min. Density of the liquid oil was measured by portable density meter (DMA 35N, Anton Paar GmbH, Graz, Austria). The hydrodesulfurization (HDS) conversion was calculated by subtracting the sulfur in the feed minus the sulfur/nitrogen in the product and divided by the sulfur/nitrogen in the feed. The calculation of rate constant *k* was based on pseudo-first-order reaction. Three catalysts CAT-270-320, CAT-20-320, and CAT-20-200, which possess the highest, moderate, and lowest HDS rates, respectively, were selected to do the reproducibility tests. At least three times were conducted for each selected catalyst. Results showed that reaction rate constants of all the tested catalysts have high reproducibility with a maximum standard deviation below 2%.

3. Results

3.1. Effect of synthesis temperature

The effect of synthesis temperature on the properties of the catalysts is first revealed from the chemical states of Mo and S atoms, using XANES spectra of S K-edge and Mo L_3-edge (Fig. 1). At S side (Fig. 1a), peak shown at 2471 eV in MoS_2 reference spectrum is attributed to the dominated electron transitions of S^{2-} valence state from 1s orbital to 3p orbital [20]. The broad peak presented at 2478–2484 eV and 2489–2495 eV is due to the S pyramidal coordination and S hexagon structure [22]. At Mo side (Fig. 1b), white lines can be observed at 2524 eV for MoS_2 reference, which is due to the electron transition of Mo^{4+} oxidation state from $2p_{3/2}$ to vacant 4d orbital [23,24]. The shoulder peak at 2532 eV is associated with the trigonal prismatic coordination of Mo atoms [23,25]. Compared to the references, at a low sTemp of 200 °C, a higher oxidation state of sulfur (S^{6+}) was indicated by the appearance of a small peak at 2483 eV. When inadequate temperature is imposed, oxygen is involved in the catalyst structure correlated with high valent sulfur. From the Mo spectra (Fig. 1b), a complete reduction of Mo^{6+} was designated by the emergence of Mo^{4+} and absence of Mo^{6+}. For catalysts synthesized at elevated temperatures (270–350 °C), similar MoS_2 profiles as reference indicate a pure MoS_2 without any oxidation state of sulfur.

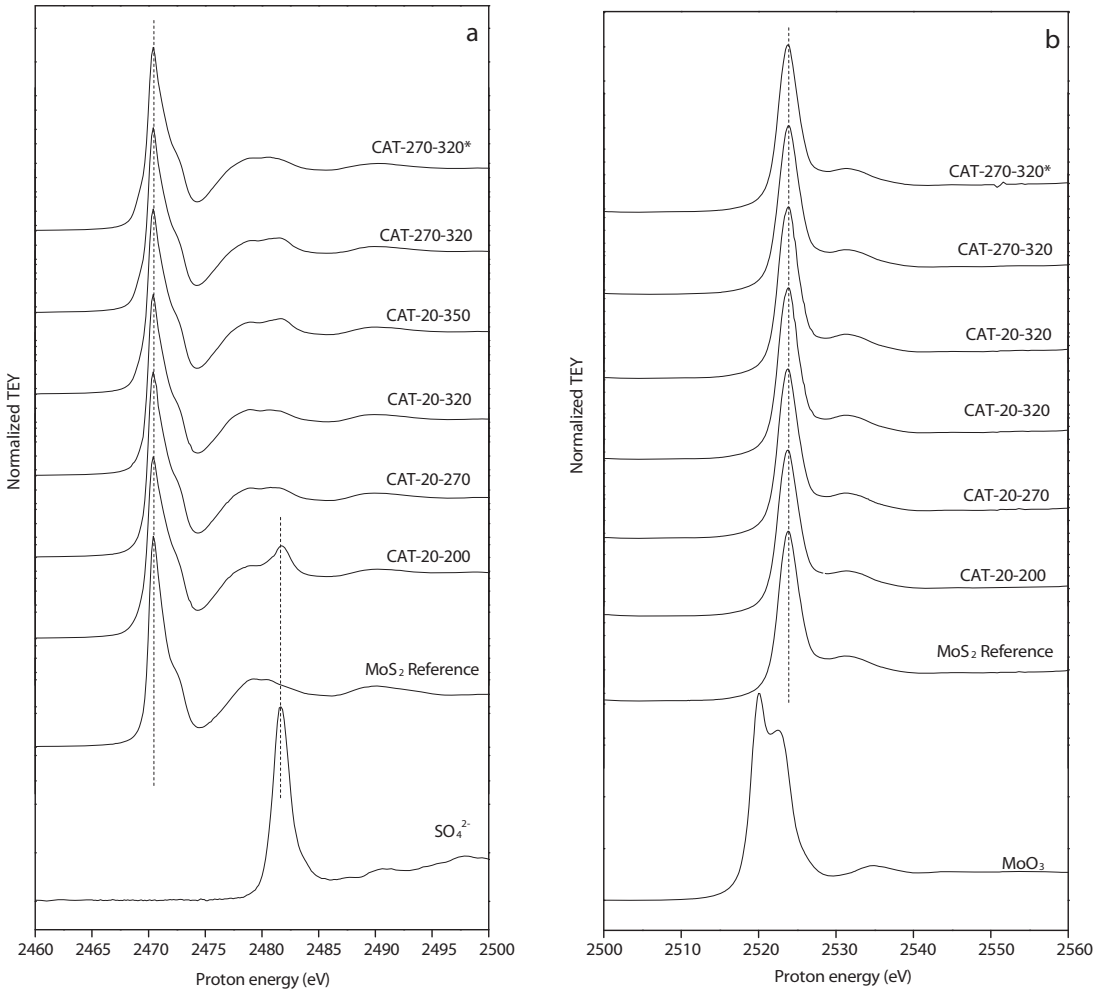

Fig. 1. XANES spectra of unsuppoted MoS_2 a: S K-edge; b: Mo L_3-edge.

Table 2
Structural parameters from the Mo K-edge Fourier-filtered k_3-weighted EXAFS of unsupported MoS_2 catalysts.

Samples	Path	CN	R (Å)	E_0 (eV)	R_f
MoS_2 reference	Mo–S	6	2.413	–	–
	Mo–Mo	6	3.166	–	–
CAT-20-270	Mo–S	4.5 ± 0.2	2.419 ± 0.004	3.3 ± 0.7	0.0053
	Mo–Mo	4.3 ± 0.3	3.184 ± 0.004		
CAT-20-320	Mo–S	4.8 ± 0.2	2.406 ± 0.005	1.7 ± 0.9	0.0071
	Mo–Mo	4.6 ± 0.4	3.171 ± 0.006		
CAT-20-350	Mo–S	5.2 ± 0.2	2.408 ± 0.006	1.2 ± 1.0	0.0103
	Mo–Mo	4.9 ± 0.4	3.171 ± 0.006		

Estimated error: $\sigma^2_{Mo-S} \pm 0.002$ Å^2, $\sigma_{Mo-Mo} \pm 0.004$ Å^2.

The crystallinity of catalysts was identified by XRD spectra (Fig. 2). At 200 °C, the emergence of 002 peak indicates a typical layered structure, whereas no discernible peaks are observed in the range of 33–58° except a board bulge, which may be derived from the merging of 100 and 103 facets. A small peak appears at 56.6°, seen as left shift of 110 lattice facets. The spectra indicate a more amorphous-like MoS_2 (a-MoS_2) structure at low temperature. When the sTemp increases to 270 °C, a crystalline structure (denoted as c-MoS_2 hereafter) starts to develop, manifested by the characteristic peaks for 002, 100, 103, and 110 facets (Fig. 2). The broad peaks, on the other hand, also reveal poor crystallite structure, which cannot be further distinguished with XRD. Detailed comparison in crystallinity is revealed by EXAFS spectra with Fourier transform of the Mo K-edge adsorption for all the three MoS_2 catalysts at elevated temperatures (Fig. 3). Each spectrum exhibits two notable peaks corresponding to Mo–S (peak A at 1.90 Å, phase shift uncorrected) and Mo–Mo (peak B at 2.86 Å, phase shift uncorrected) [25]. These peaks are due to the presence of sulfur atoms in the first coordination sphere around Mo atoms, and the nearest neighbor Mo atoms, respectively. Detailed curve fitting with bulk MoS_2 provides Mo–S and Mo–Mo structural parameters (Table 2). The Mo–S and Mo–Mo bond distances of all the catalysts are close to the bulk MoS_2 standard. Mo–S and Mo–Mo coordination numbers (CN) at three temperatures are lower than six, similar to other literatures [26]. The deviation of CN from bulk MoS_2 is attributed to the disorder of atomic arrangement. The CN is increased with the elevation of sTemp, indicating the catalyst crystallite structure is better developed at higher temperature, being more close to bulk MoS_2 phase [27].

The morphologies of the catalysts were revealed by electron microscopy techniques. Both catalyst particles are within the nanoscale with an average size lower than 200 nm (Fig. 4). CAT-20-200 seems to have a smaller size (50–100 nm) than that of CAT-20-320 (100–200 nm). An apparent difference was observed from the particle morphologies. No wire-like structure was generated at the lower synthesis temperature (CAT-20-200), and the outer contour of the particles is spherical, whereas SEM images of CAT-20-320 show flower-like structures with associated needle-like MoS_2 crystalline.

Corresponding to the different morphologies, distinct pore size distribution is observed (Fig. 5). Two main pore sizes centered at 2–3 nm and 12–15 nm are shown for the catalysts synthesized at temperature 270–350 °C and only one broad peak appears at 2–3 nm for CAT-20-200. The smaller pores at 2–3 nm are the fine intra-aggregated pores from the material and the broad peak at larger size of 12–15 nm is attributed to the secondary pores from the combination of primary particles. The lack of large pores for CAT-20-200 is attributed to the smooth appearance of primary particles. Correspondingly, a-MoS_2 shows a low BET surface area of 84.5 m^2/g (Table 1). c-MoS_2, on the other hand, with dendritic

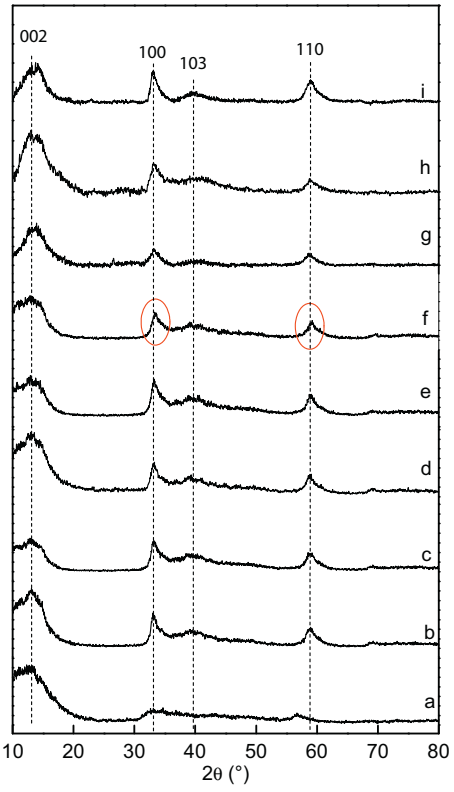

Fig. 2. XRD spectra of synthesized MoS_2; a: CAT-20-200; b: CAT-20-270; c: CAT-20-320; d: CAT-20-350; e: CAT-270-320; f: CAT-270-320*; g: spent CAT-20-200; h: spent CAT-20-270; i: spent CAT-20-320.

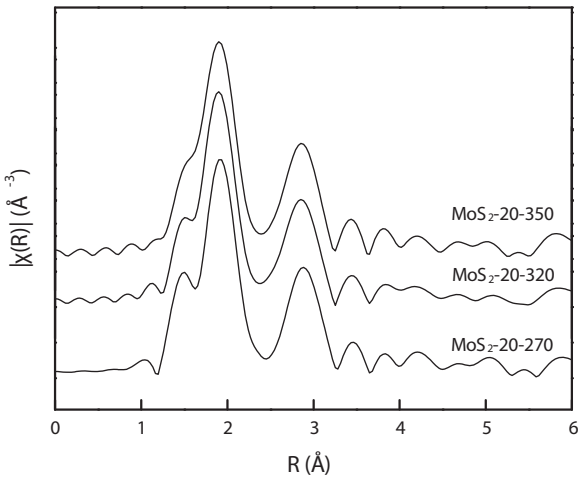

Fig. 3. Fourier transformed EXAFS spectra of unsupported MoS_2.

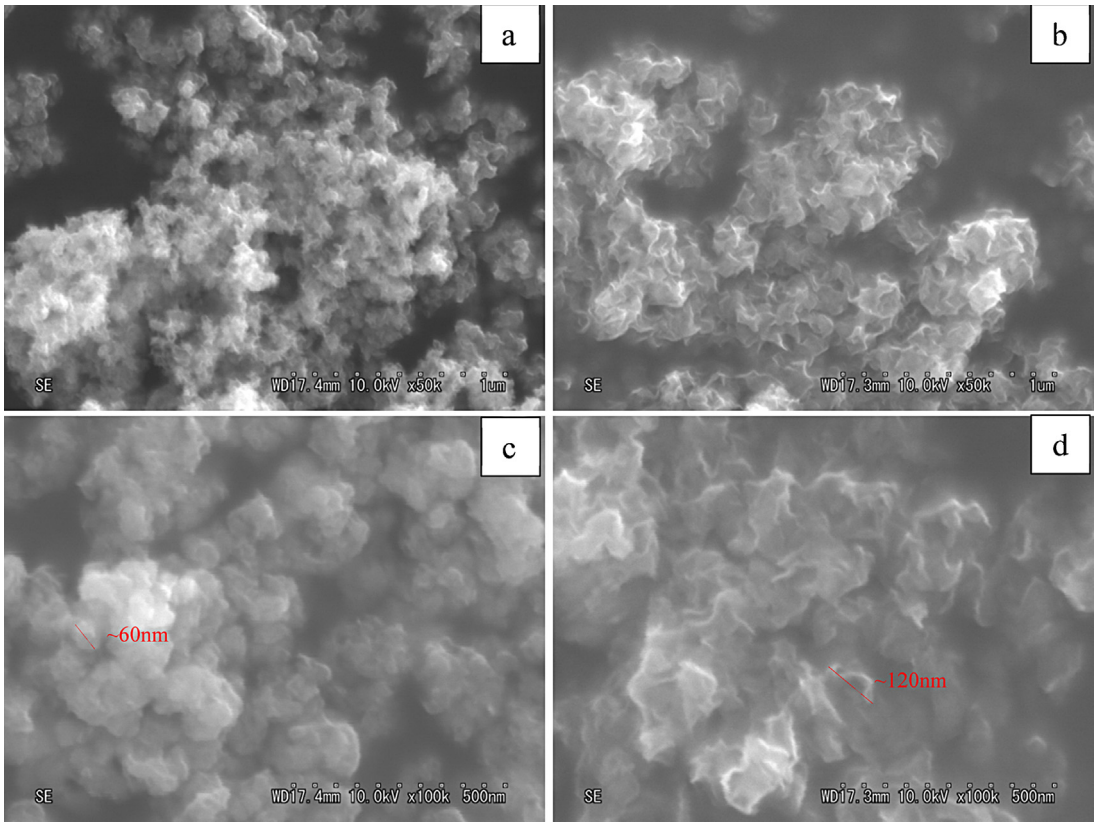

Fig. 4. SEM images of unsupported catalysts. a,c, CAT-20-200; b,d, CAT-20-320.

structure, has great tendency to form secondary pores and exhibits high surface area in the range of 155.9–261.9 m^2/g.

Crystal structure was observed from TEM images (Fig. 6). At 200 °C, short MoS_2 slabs can be seen in the bulk of amorphous MoS_2 with an average length of 5.34 nm (Fig. 6a). The full conversion of a-MoS_2 to c-MoS_2 occurs at a higher temperature (≥270 °C) (Fig. 6b–d). Catalysts synthesized at 270 °C and 320 °C are both presenting highly dispersed dendritic morphologies and layered nanocrystallines. Clear crystalline in the TEM images indicates the high purity of c-MoS_2, which is consistent with the XRD results. An increasing trend of length is found with the increase of temperature in the range of 200–320 °C. Similar phenomenon was also observed from other work when synthesizing nano-crystalline MoS_2 from

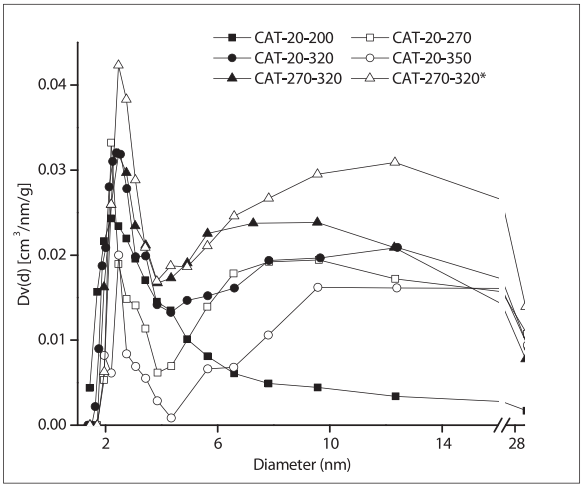

Fig. 5. Pore size distribution of unsupported catalysts.

200 to 225 °C using ammonium tetrathiomolybdate as the precursor [28]. Further increasing the temperature to near-critical temperature 350 °C, on the other hand, shortens the length of the c-MoS_2 from 17.94 nm to 11.34 nm (Fig. 6d).

As well known, MoS_2 is a highly anisotropic layered material and the crystal growth occurs in parallel (length) and perpendicular directions (stacking) [29]. In the perpendicular direction, stacked multiple layers are bonded by weak Van der Waals forces. From Table 1, it can be seen that growth preferences are distinct for catalysts prepared at different synthesis temperatures. At a low temperature of 200 °C, the growth of each face is more balanced, shown as a low L/T ratio of 2. At elevated temperatures (≥270 °C), when adequate energy is provided, the growth of the 002 face becomes dominant, evidenced by the high L/T ratio (L/T: around 7). In the developing of basal plane at 320 °C, it is also noted that the curvature of MoS_2 slab is significantly higher than of at 270 °C, as seen from Fig. 6c with a bending angle of 136–138°.

3.2. *Effect of initial temperatures*

The initial temperature (iTemp) is the start point for the synthesis of a crystalline catalyst. It becomes an important factor for the synthesis of a good catalyst as it determines the initial energy status of synthesis environment. The effect of iTemp on the chemical state of the molybdenum and sulfur species of catalysts was examined using XANES and XPS techniques. In the XANES spectra, no Mo or S valences were detected except for Mo^{4+} and S^{2-} as compared to the typical MoS_2 profile (Fig. 1). Similar conclusions can also be drawn from XPS spectra. The profiles of S 2p orbital and Mo 3d orbital are exihibted in Fig. 7. Typical peaks for S^{2-} ion and Mo^{4+} are observed at 161.8 eV and 163.0 eV for S 2p core, and at 229.0 eV and 232.1 eV for Mo 3d core, respectively [30–32]. Additionally, typical MoS_2 diffraction peaks were observed from XRD

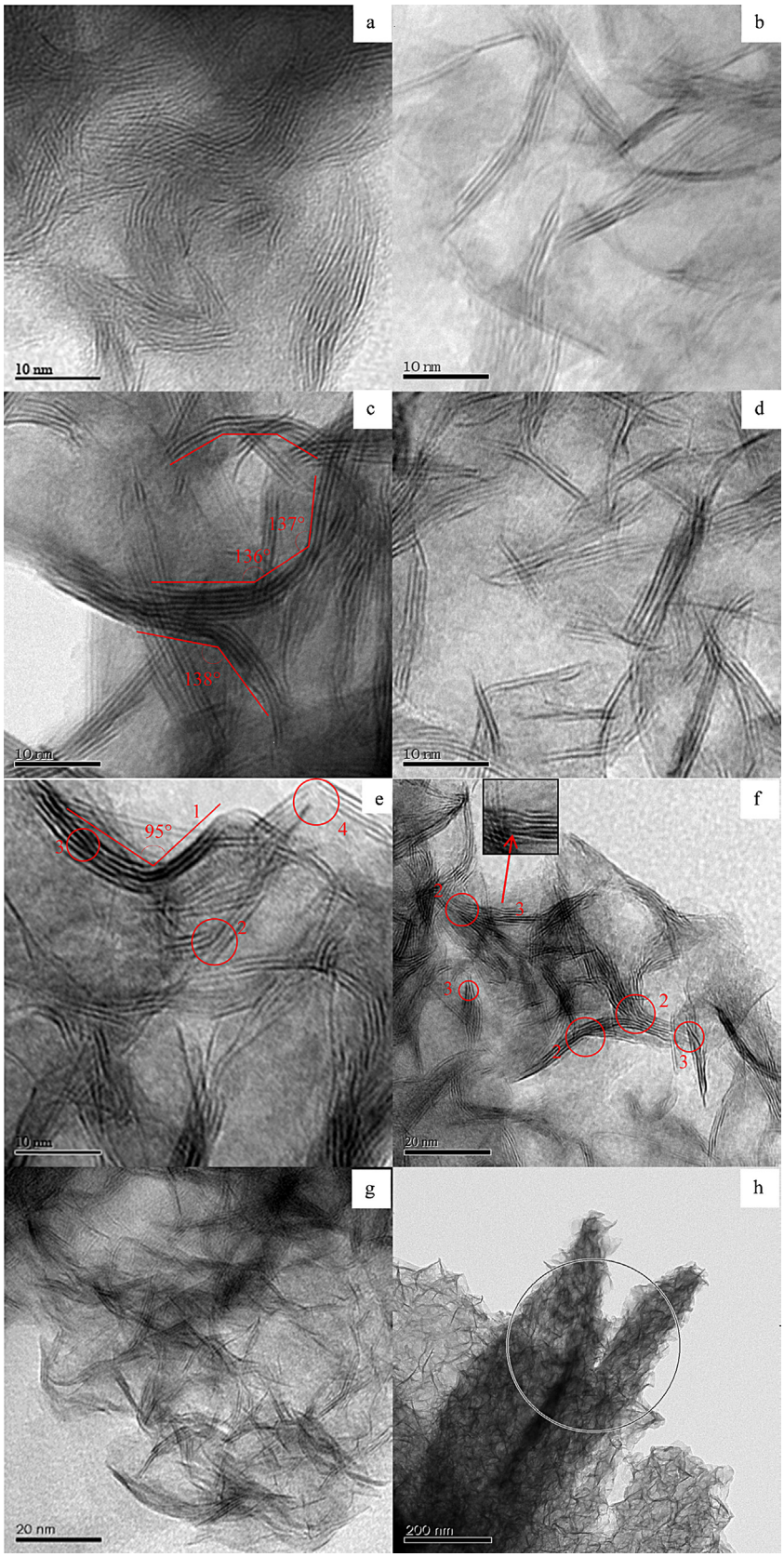

Fig. 6. TEM images of unsupported catalysts, a. CAT-20-200; b: CAT-20-270; c: CAT-20-320; d: CAT-20-350; e, f: CAT-270-320; g, h: CAT-270-320*.

Table 3
XPS binding energies for unsupported MoS_2.

Catalysts	Binding energy BE (eV)				BEs difference (eV)
	S $2p_{3/2}$	S $2p_{1/2}$	Mo $3d_{5/2}$	Mo $3d_{3/2}$	Mo $3d_{5/2}$–S $2p_{3/2}$
CAT-20-320	161.8	163.0	229.0	232.1	67.2
CAT-270-320	161.8	163.0	229.0	232.1	67.2
CAT-270-320*	161.9	163.1	229.1	232.2	67.2

spectra for catalysts under different iTemps with no significant differences (Fig. 2). These results indicate that the iTemp does not affect the molybdenum and sulfur state, and the crystal structures can be generated—as long as the minimum synthesis temperature is exceeded.

TEM pictures clearly showed high purity of c-MoS_2 structures for different iTemps. The effect of iTemp on crystallinity can be determined from the average slab length and thickness (Table 1). Both the statistical slab length and thickness decreased significantly with the increase in iTemp from 20 to 270 °C. The rapid development of a crystalline structure not only leads to short slabs, but also largely influences the crystal morphology. At a high initial temperature, the consequent growth following nucleation also occurs in an exceedingly high rate. Compared to the gradual heating protocol of CAT-20-320, more local defects were created, e.g., curvatures with sharper angles (circle 1), crystalline separation or merging (circle 2), slab growing together and lattice distance variation (circle 3), and rough edges (circle 4).

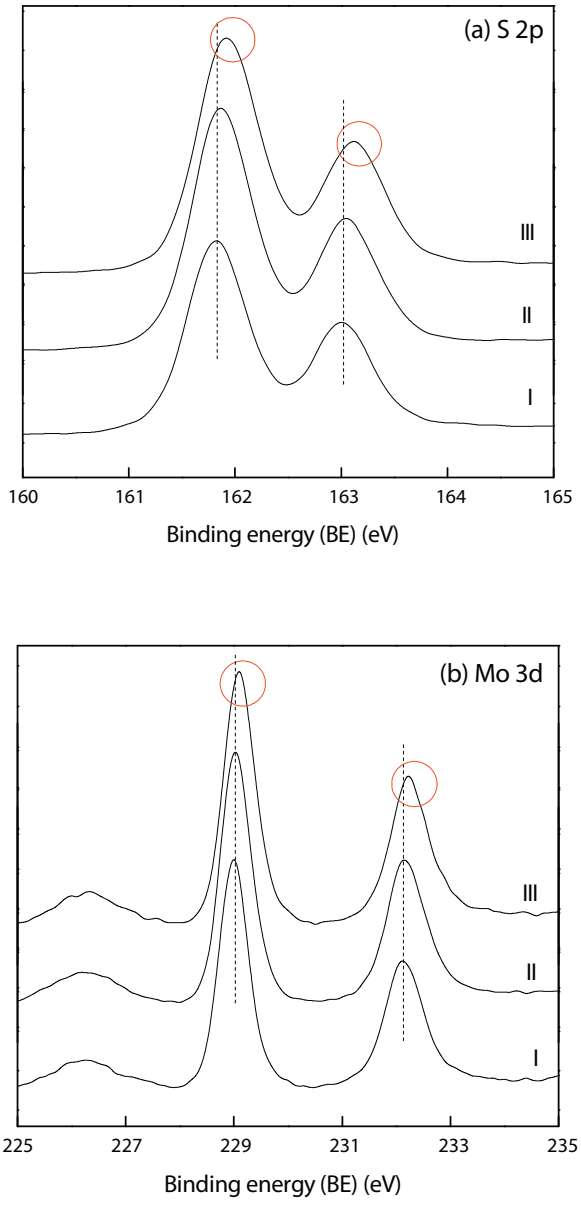

Fig. 7. XPS spectra in the binding energy (BE) range around S 2p (a) and Mo 3d (b). Spectra I, II, III refer to CAT-20-320, CAT-270-320, and CAT-270-320*, respectively

To better understand the speciality of enhanced initial temperature, the time evolution of crystalline development was studied. The synthesis of CAT-270-320a* is forced to stop as soon as the setting sTemp is reached. Incomplete-sulfided stick-like MoO_x structures were observed from TEM images (Fig. 6h, circled) and evidenced by EDX spectra with the presence of oxygen peak and lowered sulfur peak compared to CAT-270-320 (Fig. S1 in Supplementary data). Since only Mo^{4+} is detected in XANES and XPS spectra, without the appearance of any other Mo oxide state (Figs. 1and 7), MoO_x is most likely in the form of MoO_2 rather than MoO_3. A further observation showed that there are identical spectra in XANES; however, there is a difference in the XPS spectra. A right shift in Mo and S peaks of CAT-270-320* is noted compared to CAT-270-320 (Fig. 7). This indicates a higher binding energy of inner electrons (Table 3). The existence of polysulfide S_n^{2-} might be one of the possible reasons [30]. The different observations from XPS and XANES indicate that the variation in chemical state is mainly on the surface, since XPS is more surface sensitive with a probing depth of 2–4 nm, while XANES, with an estimated probing depth of 100 nm, is more bulk sensitive [20]. When the reaction proceeds, MoO_x is fully sulfided and pure MoS_2 is generated.

From XRD results, the lattice distance at time zero is deviated from the mature crystalline. The 100 and 110 peaks shift to the left and the distance *d* is correspondingly smaller (Fig. 2, Table 4). With the prolonged reaction time, the crystal is further developed in crystallinity. This is evidenced by the rectified lattice distance after 2 h reaction. It is worth noting that there are still more local defects on CAT-270-320 than the gradual heat-up (CAT-20-320), although the main lattice structure is identical.

3.3. *Hydrotreating Activity of MoS_2 on LCO*

The synthesized MoS_2 catalysts are evaluated by hydrodesulfurization tests on LCO. Table 5 shows the pseudo-first-order HDS and HDN activity of unsupported MoS_2 catalysts (HDS and HDN conversions are listed in Fig. S2 in Supplementary data). Compared with model oil, the composition of LCO is more complex, containing both easy (benzothiophene, alkyl-benzothiophene) and hard sulfur (dibenzothiophene, alkyl-dibenzothiophene) compounds, as well as nitrogen compounds (Table S1 in Supplementary data). Thus, the

Table 4
d Values (Å) at different initial and synthesis temperatures.

Catalysts	*d* Values (Å)	
	(100)	(110)
CAT-20-320	2.71	1.56
CAT-270-320	2.71	1.56
CAT-270-320*	2.67	1.57

Table 5
Kinetic data for HDS activity on real feed at 375 °C with catalyst to oil ratio of 1:200.

Catalysts	Rate constant (10^{-5} s^{-1} $gcat^{-1}$)		
	HDS (0–1 h)	HDS (1–8 h)	HDN (0–8 h)
CAT-20-200	19.3	5.3	3.2
CAT-20-270	23.3	5.9	9.9
CAT-20-320	28.6	6.6	15.5
CAT-20-350	45.2	6.8	30.0
CAT-270-320	54.9	11.4	47.0
CAT-270-320*	34.5	8.3	22.8

reaction is divided into two phases (0–1 h and 1–8 h) for the varied rate constants when eliminating S with different difficulties. Within all the catalysts prepared, the HDS kinetic rate constants vary in 19.3–54.9 and 5.3–11.4 $\times 10^{-5}$ s^{-1} $gcat^{-1}$ in the first hour and following run, respectively. As the sTemp increases from 200 to 350 °C, the initial HDS rate constant significantly increases from 19.3 to 45.2 $\times 10^{-5}$ s^{-1} $gcat^{-1}$. The effect of iTemp has a similar trend as sTemp as such that the HDS increases significantly from 28.6 to 54.9 $\times 10^{-5}$ s^{-1} $gcat^{-1}$ when the iTemp increases. HDN activity follows the same trend with HDS. The hydrocracking ability is described by boiling point distribution obtained from simulated distillation, as shown in Fig. S3 in Supplementary data. For each catalyst, the fraction of boiling point below 250 °C largely increases at the expense of fraction above 250 °C, indicating the occurrence of hydrocracking. Higher hydrocracking ability was obtained when the synthesis temperature and initial temperature were increased.

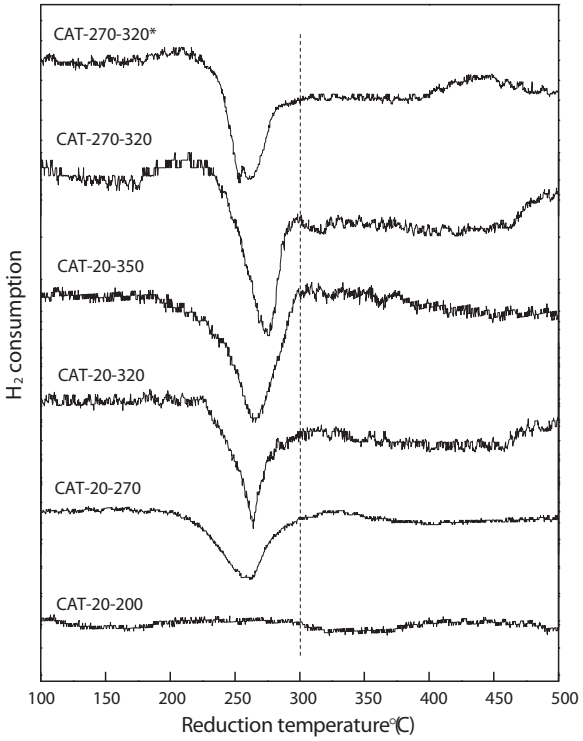

Fig. 8. H_2 consumption during TPR treatment for catalysts synthesized with different sTemp and iTemp.

4. Discussion

4.1. Crystallization process

The formation of crystalline MoS_2 from oxide precursor is a reactive crystallization process, including nucleation and consequent growth. The roles of iTemp and sTemp in each stage may significantly affect the crystallization process, which results in distinguished characteristics for the catalysts. Furthermore, those characteristics may significantly impact the catalytic activity of MoS_2.

As iTemp determines the energy status in the beginning of the reaction, it takes more effect on the nucleation stage. With high iTemp, the supersaturation state is enhanced, which decreases the nucleation energy barrier according to the nucleation theory [12]. In addition, higher iTemp provides sufficient energy to overcome the potential barrier for the creation of nuclei. Both effects lead to a mass generation of nuclei. In such case, the main route for the growth of a crystalline structure is likely to follow the combination of the nuclei (or joint segments) (Scheme 1). Through this route, the obtained slabs exhibit more disordered pattern on the basal plane, which are derived from the imperfect combination of nuclei. Several examples can be found from deformed slabs in TEM images (circled area in Fig. 6e and f). Another piece of evidence can be found by TPR spectra (Fig. 8). Catalysts with high iTemp show a different H_2 consumption shape at high reduction temperature range, which is hardly distinguished as a "peak", but rather a flat area. This H_2 consumption is attributed to the defect sites on the basal plane. Unlike more uniform edge structures, which require similar energy showing a shape peak on TPR spectra, the active sites on the basal plane tend to vary, leading to a broad adsorption area in terms of temperature. It was also observed that the H_2 adsorption capability over 300–500 °C increased for the catalysts synthesized at higher iTemp, corresponding to the higher fraction of defects on the basal plane. Additionally, the combination of nuclei is likely to form slabs with limited length, since the connection of segments is more difficult than monomers.

The development of crystals in the combination route is seen from the comparison of CAT-270-320 and CAT-270-320*. For CAT-270-320*, crystallization is forced to stop before the segments join appropriately. This leads to the presence of large number of segments, which is shown with the deformed d-space in XRD spectra. The crystal can further develop with exposure to sTemp for a sufficient amount of time. As the thermal vibration continues to provide energy to the system, atoms on the edge of segments can be activated to overcome the surface potential and easier to connect to other segments. Thus, some imperfections on the joint points can be rectified. Longer slabs are also observed in CAT-270-320, indicating that sTemp may promote the combination process (Table 1).

In the situation of low iTemp, chemical reaction occurs in a moderate circumstance, resulting in a relative low supersaturation state. Fewer nuclei will be formed and monomers are more likely to attach on the existing nuclei rather than creating new

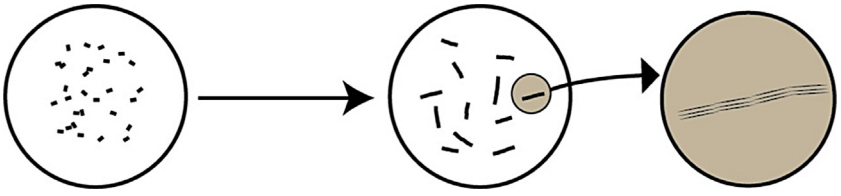

Scheme 1. Route of combination of nuclei.

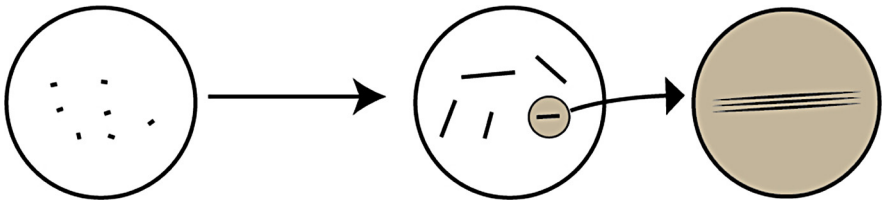

Scheme 2. Route of continuous growth.

ones. Thus, the growth of crystal is mainly through the continuous growth of individual nuclei (Scheme 2). Compared to nuclei (or joint segments), monomers are smaller and more flexible, and thus easier to attach on the correct positions. Therefore, the crystallinity of MoS_2 formed via continuous growth is generally more complete than the combination of nuclei. This is demonstrated by the TEM images which show parallel slabs and fewer basal defects (Fig. 6b–d). The role of continuous growth can also be revealed by TPR spectra (Fig. 8). With higher crystallinity on the basal, catalysts synthesized with low iTemp only show a small peak at higher reduction temperature range (>300 °C), indicating less active sites on basal (except CAT-20-320 due to the curvature). In contrast, large peaks are found in the reduction temperature of 200–300 °C, which refers to the S coverage on the edges and rims.

In the development of crystals through continuous growth, the crystallinity of a MoS_2 sheet is improved by the appropriate attachment of monomers. The elevation of temperature increases the kinetic energy of monomers to overcome the potential barrier and move to the lattice position, and thus facilitates the growth in a more ordered pattern. The enhanced crystallinity is evidenced by XRD and EXAFS results (Fig. 2, Table 2). Unlike segment combination route, the increase of slab length is through the accumulation of monomers on the growing surface. With the increase of sTemp, the growth rate will be enhanced, leading to longer slabs, as is shown by longer slabs developed at 320 °C compared to 270 °C. A higher curvature degree is also observed on CAT-20-320. This is probably because that morphological instability would occur on the growing rough interface at higher growing rate, which led to branching and curving [10].

The speciality of shorter slabs of CAT-20-350 is probably due to the characteristics of water in near-critical region, where advanced nucleation competes with the growth of MoS_2 basal plane. At or near-critical point, specific characteristics are present, e.g., low dielectric constant, low surface tension, low solubility, high reaction rate, and diffusivities, etc., [33–35]. At 350 °C, the water would partially possess the characteristics of supercritical water. With these properties, the interfacial energy will be dramatically lower, and a large supersaturation will be generated leading to a higher nucleation rate (secondary nucleation) competing with the growth of MoS_2 slab.

It is worth noting that crystals cannot be developed with insufficient sTemp. At 200 °C, the formation of amorphous material is more kinetically favorable due to the low supersaturation [36]. Without adequate driving force, molybdenum sulfide tends to grow in a less ordered way to lower the growth resistance. In this case, the growth leads to a more amorphous-like MoS_2, which is indicated by the existence of high valent sulfur S^{6+}. Without an ordered atomic arrangement, oxygen has higher tendency to be present in the distorted structure, which may further lower the crystallinity (Fig. 1). In addition, MoS_2 with inadequate energy prefers to grow in perpendicular direction and forms shorter and thicker slabs, because superposition of layers with Van der Waals forces in the perpendicular direction requires less energy than development of basal plane (002).

4.2. Relationship between properties and activity

The catalytic activities of MoS_2 are highly influenced by sTemp and iTemp through the impact of crystal properties such as crystallinity, crystal size, and morphology. Crystallinity is essential to provide suitable structure to create active sites and high surface areas, which can be illustrated by the low hydrotreating performance of CAT-20-200 that does not have a crystal structure. It is also observed that the activity is increased with the improvement of crystallinity after crystal structure is generated. A possible reason may be related to the ability of providing structural sulfur. When the crystallinity is low, amorphous structures are generally exhibited on the edge sites, since the fully saturated basal plane is expected to be better arranged. Consequently, amorphous structure on the edge may decrease the efficiency of creating accessible structural sulfur deficiency. No obvious differences were observed in the XRD patterns of all the catalysts except CAT-20-200 in which MoS_2 grew from amorphous to crystalline structure after high temperature HDS reaction. It indicates that the crystallization structure is robust if good crystallinity is obtained during synthesis.

Crystal size and morphology play an important role in generating sufficient amount of active sites. Based on the characterization and HDS evaluation, it is found that catalytic activity is enhanced with shorter slab and larger curvatures, regardless of the sTemp or iTemp. For example, the better performance is observed with catalysts of the shorter slabs (CAT-20-350) or curved (CAT-20-320). The highest activity is obtained from CAT-270-320 that possesses both characteristics. This observation is consistent with the other statements that the active sites are located on the edge and curved basal plane [37,38]. The exception of a lower activity of CAT-20-320* with shortest slabs compared to CAT-270-320 is mainly due to the impurity of MoO_x and distorted structure. However, it is worth noting, in spite of impurity, CAT-20-320* still exhibits a fair activity due to extensive sites on the edge and basal plane. The selected spent catalysts, except CAT-20-200, show unnoticeable change on their morphology compared to that of the corresponding fresh catalysts (Table 1). It suggests that the MoS_2 catalyst synthesized through the hydrothermal approach is durable.

5. Conclusions

A series of unsupported MoS_2 catalysts were synthesized via a novel hydrothermal method. Commercial available Na_2S and MoO_3 were employed as precursors. The synthesis temperature and initial temperature show great influence on crystallization process and catalyst properties. There are two molybdenum sulfide states detected: amorphous (a-MoS_2) and nanocrystalline MoS_2 (c-MoS_2). At low temperature of 200 °C, amorphous a-MoS_2 is formed with inadequate sulfuration. The full conversion to c-MoS_2 was achieved after 270 °C. The growth of c-MoS_2 follows different crystallization routes, including nuclei combination and continuous growth. Higher iTemp favors the first route, in which shorter and defected slabs are generated. At lower iTemp, catalyst is more likely grown in the second way, leading to fewer defects on the basal plane. In continuous growth, with the increase of sTemp from

270 °C to 320 °C, the slabs tend to grow longer and curved; further increase of temperature to near-critical temperature 350 °C, the slab length decreases due to the competition with secondary nucleation.

The performance of catalysts was evaluated using light cycle oil. Results show MoS_2 prepared at higher synthesis temperature and initial temperature exhibits higher HDS and HDN activities. The HDS (BTs) rate constant of MoS_2 synthesized at 350 °C (CAT-20-350) is more than two times of that at 200 °C (CAT-20-200). Furthermore, the HDN rate constant of CAT-20-350 is nearly 10 times greater than that of CAT-20-200. Similarly, the HDS and HDN rate constants of MoS_2 prepared at an iTemp of 270 °C are nearly 2 times of the one starting at 20 °C. The low activity of CAT-20-200 is mainly due to its amorphous structure. The increase of c-MoS_2 activity with sTemp is attributed to the curved/shortened MoS_2 slabs and enhanced crystallinity. Both edge sites and basal defects contribute to the high activity of CAT-270-320.

Acknowledgments

The authors gratefully acknowledge the financial assistance from Canada Research Chairsprogram, Natural Sciences and Engineering Research Council of Canada and Canada Foundation for Innovation.

Appendix A. Supplementary data

Supplementary data associated with this article can be found, in the online version, at http://dx.doi.org/10.1016/j.apcatb.2014.10.046.

References

[1] G.A. Camacho-Bragado, J.L. Elechiguerra, A. Olivas, S. Fuentes, D. Galvan, M.J. Yacaman, J. Catal. 234 (2005) 182.
[2] D. Mahajan, C.L. Marshall, N. Castagnola, J.C. Hanson, Appl. Catal. A 258 (2004) 83.
[3] M. Kouzu, K. Uchida, Y. Kuriki, F. Ikazaki, Appl. Catal. A 276 (2004) 241.
[4] T.C. Ho, J.M. McConnachie, J. Catal. 277 (2011) 117.
[5] Y. Yi, B. Zhang, X. Jin, L. Wang, C.T. Williams, G. Xiong, D. Su, C. Liang, J. Mol. Catal. A: Chem. 351 (2011) 120.
[6] C. Wang, Z. Wu, C. Tang, L. Li, D. Wang, Catal. Commun. 32 (2013) 76.
[7] B. Yoosuk, J.H. Kim, C. Song, C. Ngamcharussrivichai, P. Prasassarakich, Catal. Today 130 (2008) 14.
[8] Y. Araki, Y. Iwata, Y. Miki, K. Honna, N. Matsubayashi, H. Shimada, in: B. Delmon, G.F. Froment, P. Grange (Eds.), Hydrotreatment and Hydrocracking of Oil Fractions, The Netherlands, Elsevier Science B.V., 1999, p. 69.
[9] E. Devers, P. Afanasiev, B. Jouguet, M. Vrinat, Catal. Lett. 82 (2002) 13.
[10] W.J. Li, E.W. Shi, J.M. Ko, Z.Z. Chen, H. Ogino, T. Fukuda, J. Cryst. Growth 250 (2003) 418.
[11] G. Madras, B.J. McCoy, Chem. Eng. Sci. 59 (2004) 2753.
[12] G. Madras, B.J. McCoy, Acta Mater. 51 (2003) 2031.
[13] J.-X. Su, X.-P. Wang, Q. Pan, W. Qu, Chin. J. Inorg. Chem. 23 (2007) 1015.
[14] J. Yu, G. Wang, B. Cheng, M. Zhou, Appl. Catal. B 69 (2007) 171.
[15] B. Akin, M. Oner, Res. Chem. Intermed. 38 (2012) 1511.
[16] G. Madras, B.J. McCoy, J. Chem. Phys. 119 (2003) 1683.
[17] Y.M. Tian, X. Zhao, L.C. Shen, F.Y. Meng, L.Q. Tang, Y.H. Deng, Z.C. Wang, Mater. Lett. 60 (2006) 527.
[18] B. Yoosuk, C. Song, J.H. Kim, C. Ngamcharussrivichai, P. Prasassarakich, Catal. Today 149 (2010) 52.
[19] H.P. Zhang, H.F. Lin, Y. Zheng, Highly dispersed nanocrystalline molybdenum sulfide prepared by hydrothermal synthesis as an unsupported model catalyst for ultra clean diesel, in: Proceedings of the 21st Canadian Symposium on Catalysis, Banff, Alberta, 2010.
[20] V.R. Surisetty, Y.F. Hu, A.K. Dalai, J. Kozinski, Appl. Catal. A 392 (2011) 166.
[21] C. Calais, N. Matsubayashi, C. Geantet, Y. Yoshimura, H. Shimada, A. Nishijima, M. Lacroix, M. Breysse, J. Catal. 174 (1998) 130.
[22] N. Dinter, M. Rusanen, P. Raybaud, S. Kasztelan, P. da Silva, H. Toulhoat, J. Catal. 267 (2009) 67.
[23] H. Aritani, T. Tanaka, T. Funabiki, S. Yoshida, K. Eda, N. Sotani, M. Kudo, S. Hasegawa, J. Phys. Chem. 100 (1996) 19495.
[24] H. Aritani, O. Fukuda, A. Miyaji, S. Hasegawa, Appl. Surf. Sci. 180 (2001) 261.
[25] Y.V. Zubavichus, A.S. Golub, Y.N. Novikov, Y.L. Slovokhotov, A.N. Nesmeyanov, P.J. Schilling, R.C. Tittsworth, J. Phys. IV 7 (1997) 1057.
[26] M. Polyakov, M.W.E. van den Berg, T. Hanft, M. Poisot, W. Bensch, M. Muhler, W. Gruenert, J. Catal. 256 (2008) 126.
[27] H.-R. Seo, Y.-K. Lee, J. Korean Phys. Soc. 59 (2011) 730.
[28] X. Bokhimi, J.A. Toledo, J. Navarrete, X.C. Sun, M. Portilla, Int. J. Hydrog. Energy 26 (2001) 1271.
[29] P. Afanasiev, C.R. Chim. 11 (2008) 159.
[30] R.S. Smart, W.M. Skinner, A.R. Gerson, Surf. Interface Anal. 28 (1999) 101.
[31] P. Afanasiev, G.F. Xia, G. Berhault, B. Jouguet, M. Lacroix, Chem. Mater. 11 (1999) 3216.
[32] L.P. Nielsen, M. Schonning, S.V. Christensen, S.V. Hoffmann, Z.S. Li, P. Hofmann, F. Besenbacher, B.S. Clausen, Catal. Lett. 73 (2001) 85.
[33] Y. Zhang, C. Erkey, J. Supercrit. Fluids 38 (2006) 252.
[34] K. Byrappa, S. Ohara, T. Adschiri, Adv. Drug Deliv. Rev. 60 (2008) 299.
[35] A. Michailovski, G.R. Patzke, Chem.—Eur. J. 12 (2006) 9122.
[36] B.D. Fahlman, What is Materials Chemistry? Springer, 2011.
[37] A. Nogueira, R. Znaiguia, D. Uzio, P. Afanasiev, G. Berhault, Appl. Catal. A 429 (2012) 92.
[38] M. Daage, R.R. Chianelli, J. Catal. 149 (1994) 414.